



Article

Facile Assembly of InVO₄/TiO₂ Heterojunction for Enhanced Photo-Oxidation of Benzyl Alcohol

Xinyu Zhang ^{1,2,†}, Quanquan Shi ^{1,†}, Xin Liu ^{1,3,*} , Jingmei Li ¹, Hui Xu ^{1,*}, Hongjing Ding ¹ and Gao Li ^{2,*} 

¹ College of Science, Inner Mongolia Agricultural University, Hohhot 010018, China; zhangxy04@yeah.net (X.Z.); qqshi@dicp.ac.cn (Q.S.); ljm19970043@163.com (J.L.); helloxiaoding@126.com (H.D.)

² State Key Laboratory of Catalysis, Dalian Institute of Chemical Physics, Chinese Academy of Sciences, Dalian 116023, China

³ Institute of Advanced Materials, College of Chemistry and Chemical Engineering, Jiangxi Normal University, Nanchang 330022, China

* Correspondence: liuxin@jxnu.edu.cn (X.L.); yqfxxuhui@163.com (H.X.); gaoli@dicp.ac.cn (G.L.)

† These authors contributed equally to this work.

Abstract: In this work, an InVO₄/TiO₂ heterojunction composite catalyst was successfully synthesized through a facile hydrothermal method. The structural and optical characteristics of InVO₄/TiO₂ heterojunction composites are investigated using a variety of techniques, including powder X-ray diffraction (XRD), transmission electron microscopy (TEM), and spectroscopy techniques. The addition of InVO₄ to TiO₂ considerably enhanced the photocatalytic performance in selective photo-oxidation of benzyl alcohol (BA). The 10 wt% InVO₄/TiO₂ composite photocatalyst provided a decent 100% BA conversion with over 99% selectivity for benzaldehyde, and exhibited a maximum conversion rate of 3.03 mmol g⁻¹ h⁻¹, which is substantially higher than bare InVO₄ and TiO₂. The excellent catalytic activity of the InVO₄/TiO₂ photocatalyst is associated with the successful assembly of heterostructures, which promotes the charge separation and transfer between InVO₄ and TiO₂.

Keywords: InVO₄/TiO₂ heterojunction; photocatalysis; oxidation; benzyl alcohol



Citation: Zhang, X.; Shi, Q.; Liu, X.; Li, J.; Xu, H.; Ding, H.; Li, G. Facile Assembly of InVO₄/TiO₂ Heterojunction for Enhanced Photo-Oxidation of Benzyl Alcohol. *Nanomaterials* **2022**, *12*, 1544. <https://doi.org/10.3390/nano12091544>

Academic Editor: Maria Violetta Brundo

Received: 5 April 2022

Accepted: 28 April 2022

Published: 3 May 2022

Publisher's Note: MDPI stays neutral with regard to jurisdictional claims in published maps and institutional affiliations.



Copyright: © 2022 by the authors. Licensee MDPI, Basel, Switzerland. This article is an open access article distributed under the terms and conditions of the Creative Commons Attribution (CC BY) license (<https://creativecommons.org/licenses/by/4.0/>).

1. Introduction

The consumption of chemical fuels results in ever-increasing environmental and energy issues; thus, developing a green and renewable energy source is essential [1–3]. Selective oxidation has been widely recognized as a promising strategy for alcohols to produce corresponding aldehydes, especially from benzyl alcohol toward benzaldehyde, which is one of the most important chemical processes in industry [4,5]. Benzaldehyde (BAD), one of the most common industrial chemicals, is widely used in the manufacturing of pharmaceuticals, perfumes, dyes, and additives [6,7]. However, several traditional thermal synthesized routes, such as the oxidation of toluene and hydrolysis of benzyl chloride, use high-valent metal salts (e.g., permanganate, dichromate) and lead to a variety of hazardous wastes [8]. Photocatalytic selective oxidation benzyl alcohol (BA) using O₂ as a green oxidant is recognized as a promising strategy for replacing traditional materials [9,10].

Among various semiconductor photocatalysts, TiO₂ has been extensively studied owing to lower cost, nontoxicity, and exceptional photocatalytic performance [11]. Nevertheless, the wider bandgap (only absorbs ultraviolet) and higher recombination rate of photogenerated electrons and holes seriously restrict its photocatalytic activity under sunlight [12]. The heterostructure composite is regarded as one of the most promising ways for harvesting sunlight and boosting the photocatalytic activity with the synergistic effects of heterogeneous interfaces between multiple semiconductors [13–15]. Oliveira et al. prepared heterojunction clusters of M@Si₁₂ (M = Ti, Cr, Zr, Mo, Ru, Pd, Hf and Os) and M@Si₁₆ (M = Ti, Zr, Hf) and studied their properties [13].

Recently, InVO_4 with a bandgap of 2.0 eV has been indicated as a novel visible-light-responsive photocatalyst [16]. The orthorhombic crystalline phase of InVO_4 consists of VO_4 tetrahedra sharing corners with InO_6 groups to form compact In_4O_6 groups [17], which recently was used for various photocatalytic reactions, such as H_2 evolution and photodegradation of organic pollutants [16,18]. However, the activity of the InVO_4 photocatalyst is not ideal due to sluggish electron mobility. Motivated by these points, we herein successfully constructed $\text{InVO}_4/\text{TiO}_2$ heterojunction composites via an in situ hydrothermal transformation of titanate nanotubes with indium nitrate, which is verified through powder X-ray diffraction, transmission electron microscopy, and spectroscopy techniques. The $\text{InVO}_4(112)/\text{TiO}_2(101)$ heterogeneous interface largely promotes the separation and transfer of photogenerated charges between InVO_4 and TiO_2 . A 10 wt% $\text{InVO}_4/\text{TiO}_2$ photocatalyst showed a maximum conversion rate of $3.03 \text{ mmol g}^{-1} \text{ h}^{-1}$. Furthermore, trapping experiments verified that the active radicals of $\cdot\text{O}_2^-$, $\cdot\text{OH}$ and h^+ are responsible for the enhanced activity. Overall, this work may provide important information for the exploration of new materials for photocatalytic oxidation of BA to BAD.

2. Materials and Methods

2.1. Preparation of Sodium Titanate Nanotube Precursor

All chemicals were commercially available as reagent grade and were used as received without further purification. Titanate nanotubes were synthesized via a facile hydrothermal method. Initially, 12 g NaOH was dissolved into 30 mL distilled water to form 10 mol L^{-1} NaOH aqueous solution in a 50 mL Teflon bottle, and 1 g P25 was added. After stirring for 30 min, the Teflon bottle was sealed tightly and heated at $120 \text{ }^\circ\text{C}$ for 24 h. The precipitate was centrifuged and washed with distilled water several times until the pH reached about 8. The obtained white precipitates were wet sodium titanate nanotubes.

2.2. Preparation of $\text{InVO}_4/\text{TiO}_2$ Heterojunction Compound Catalyst

$\text{InVO}_4/\text{TiO}_2$ composite photocatalysts were prepared via a simple hydrothermal reaction of sodium titanate nanotubes with InCl_3 in the presence of NH_4VO_3 . Typically, a certain proportion of NH_4VO_3 and InCl_3 was dissolved in 30 mL distilled water, and then pH was adjusted to 1–2 using nitric acid. Next, 1 g of sodium titanate nanotubes was dispersed to the former suspension under vigorous stirring. After 30 min, the slurry was transferred into autoclaves and heated at $180 \text{ }^\circ\text{C}$ for 18 h. The obtained precipitate was washed with water and dried at $80 \text{ }^\circ\text{C}$ for 12 h. Additionally, by controlling additional amounts of InCl_3 and the titanate nanotubes, different ratios of $\text{InVO}_4/\text{TiO}_2$ heterojunction composite catalysts were obtained and denoted as InTi-x (x represents the weight amount of InVO_4 , e.g., 5, 10, and 15). The InVO_4 samples were prepared via similar procedures in the absence of titanate nanotubes.

2.3. Catalyst Characterization

Powder X-ray diffraction (XRD) patterns were performed using a PANalytical Empyrean diffractometer operated at 40 kV and 200 mA. Transmission electron microscopy (TEM) images were recorded using field emission transmission electron microscopy (FEI Tecnai F20). Specific surface areas were determined using nitrogen adsorption at 77K and the BET method. Pore size distributions were derived from nitrogen desorption isotherms using the Barrett-Joyner-Halenda (BJH) method. Fourier transform-infrared (FTIR) spectra were obtained using a Perkin-Elmer Spectrum 100 Spectrometer at room temperature. X-ray photoelectron spectra (XPS) were tested on an ESCALAB MK-II spectrometer (VG Scientific Ltd., London, UK) with Al $\text{K}\alpha$ radiation. UV-visible diffuse reflectance spectra were recorded in the range of 200–800 nm on a spectrophotometer (PE Lambda 850) using BaSO_4 as a reference. Photoluminescence (PL) spectra were operated at room temperature on a fluorescence lifetime spectrophotometer (Hitach, F4600, Japan). The photoelectrochemical tests of samples were carried out on an electrochemical workstation (CHI760E, Shanghai) with a standard three-electrode system, including an Ag/AgCl electrode and a Pt plate as

the reference and counter electrodes. The as-obtained samples were coated on FTO glass substrates to be used as the working electrodes. A 300 W Xe lamp with a cut-off filter ($\lambda > 420$ nm) was used as the light source, and all of the electrochemical tests were carried out in $\text{KH}_2\text{PO}_3\text{-K}_2\text{HPO}_3$ buffer solution (0.5 M, pH = 7).

2.4. Catalytic Tests

Photocatalytic oxidation of benzyl alcohol was carried out in a stainless steel autoclave. Typically, 50 mg of catalyst, 40 μL of benzyl alcohol, and 20 mL of acetonitrile were added to a reactor. Next, the autoclave was filled with pure oxygen of 0.5 MPa and then was irradiated with a 300 W xenon lamp at a stirring rate of 500 rpm. After the reaction, the mixture was centrifuged to obtain the supernatant, which was analyzed by gas chromatographic (Agilent 7820 GC) analysis. Furthermore in the cycle stability test, the used catalysts were centrifuged, washed, and dried for the next run. In a free radical capture experiment, 20 μL Isopropanol (IPA), ammonium oxalate (AO), and 1,4-benzoquinone (BQ) were added respectively as scavengers of hydroxyl radical ($\cdot\text{OH}$), hole (H^+) and superoxide radical ($\cdot\text{O}_2^-$).

3. Results

3.1. Synthesis and Characterization of $\text{InVO}_4/\text{TiO}_2$ Nanocomposites

$\text{InVO}_4/\text{TiO}_2$ nanocomposites were prepared based on the $\text{Na}_2\text{Ti}_3\text{O}_7$, nanotubes were dissociated and transformed into TiO_2 nanoparticles, and the InVO_4 nanoparticles were simultaneously grown and anchored onto the TiO_2 surface. The phase composition and crystal structure of the prepared sample were characterized by power XRD. Figure 1a shows that the diffraction peaks of pure TiO_2 could be indexed to anatase- TiO_2 [19]. Bare InVO_4 could be indexed to the orthonormal phase with the diffraction peaks at 18.5, 20.8, 31.1, 33.0, 41.6, 51.0, and 60.9°, corresponding to (110), (020), (200), (112), (202), (042), and (242) crystal facets of InVO_4 (JCPDS 48-0898) [20]. For the InTi-x composites, all diffraction lines match well with the feature lines of InVO_4 and TiO_2 , and no diffraction peaks of other species were found, which indicates the formation of a heterojunction structure.

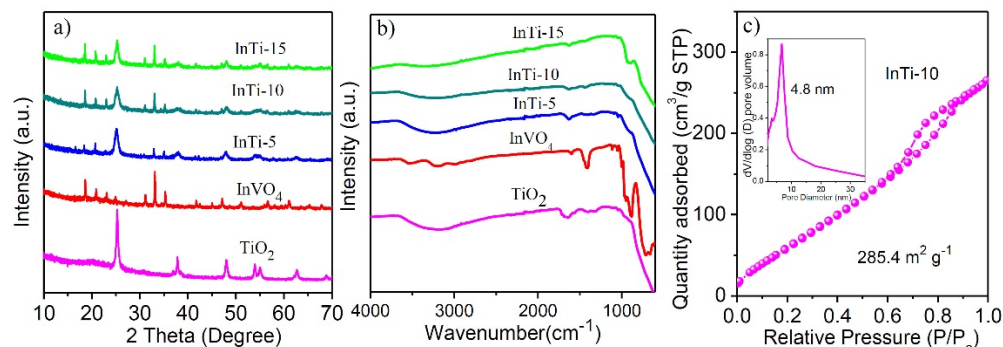


Figure 1. (a) XRD patterns and (b) FT-IR spectra of bare TiO_2 and InVO_4 and InTi-x composites. (c) N_2 -adsorption-desorption isotherms of InTi-10 composites.

Figure 1b shows the Infrared spectra of TiO_2 , InVO_4 , and InTi-x . IR peaks of TiO_2 at 3260 cm^{-1} and 1655 cm^{-1} were ascribed to O-H (tensile mode) and Ti-OH (bending mode), respectively [21]. Pure InVO_4 displayed significant peaks at 896 cm^{-1} and 631 cm^{-1} , which were related to V-O and V-O-In bonds, respectively [22,23]. The IR peaks of InTi-x composites were consistent with vibration peak of InVO_4 and TiO_2 , proving the successful coupling of TiO_2 and InVO_4 . Further, the InTi-10 sample exhibited a typical IV isotherm and a large surface area of 285.4 $\text{m}^2 \text{g}^{-1}$ (Figure 1c) [24].

The morphological characteristics of $\text{InVO}_4/\text{TiO}_2$ composite were studied by TEM (Figure 2). Figure 2a showed that InTi-10 composite is composed of particles with diameters of 10–20 nm. In addition, TiO_2 and InVO_4 were evenly distributed, and abnormally large particles were not observed. Figure 2b clearly shows the interface between TiO_2 and InVO_4 ,

where the lattice spacing of TiO_2 and InVO_4 was 0.35 nm and 0.27 nm, corresponding to $\text{TiO}_2(101)$ and $\text{InVO}_4(112)$ planes, respectively [25]. The morphology of connected particles between InVO_4 and TiO_2 indicated the existence of a $\text{InVO}_4/\text{TiO}_2$ heterojunction.

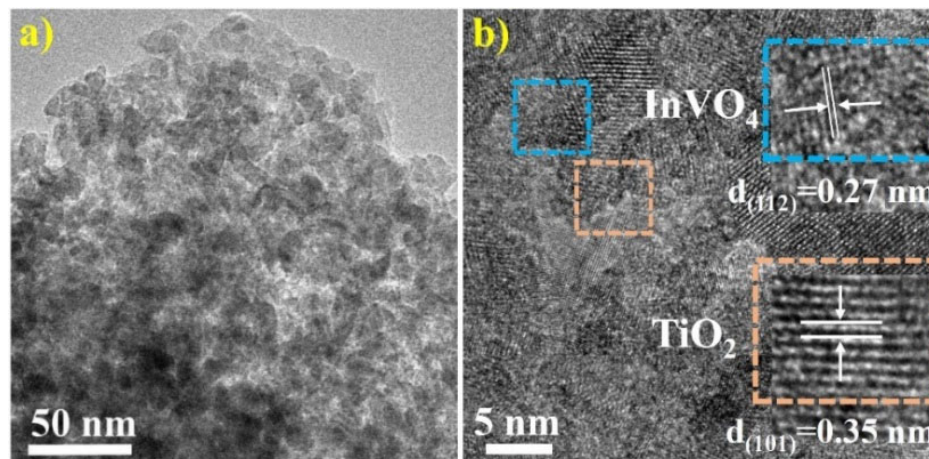


Figure 2. (a) TEM images and (b) HRTEM of InTi-10 composites.

X-ray photoelectron spectroscopy (XPS) was employed to investigate the valence states of TiO_2 , InVO_4 , and InTi-10 composites. Figure 3 depicts the XP spectra of In3d, V2p, Ti2p, and O1s. Figure 3a shows two distinct peaks at 452.8 eV (In $3d_{5/2}$) and 445.2 eV (In $3d_{3/2}$), associated with In^{3+} [26]. Two characteristic binding energies (BEs) at 524.9 eV and 517.4 eV in InVO_4 correspond to V $2p_{3/2}$ and V $2p_{1/2}$, respectively, which are related to V^{4+} species (Figure 3a) [27,28]. For InTi-10 composites, slight shifts were seen, which indicate a strong interaction between InVO_4 and TiO_2 . Two binding energies (BEs) were found at 458.5 eV and 464.2 eV in both TiO_2 samples, which are assigned to Ti $2p_{3/2}$ and Ti $2p_{1/2}$ and correspond to Ti^{4+} species (Figure 3c) [29,30]. It was also noted that two characteristic peaks for InTi-10 composites could be identified; the peaks at 457.4 eV (Ti $2p_{3/2}$) and 463.1 eV (Ti $2p_{1/2}$) are assigned to Ti^{3+} [5]. The O 1s spectrum in the TiO_2 sample consists of two types of oxygen species. The BEs at 529.9 and 531.4 eV (Figure 3d) are ascribed to lattice oxygen (O_L) and oxygen vacancies (O_v), respectively [31–33]. Moreover, another oxygen species for bare InVO_4 and InTi-10 composites have appeared with BEs at 532.1 eV, which correspond to hydroxyl groups (O_H) on the oxide surface. Consequently, the obtained results revealed that InTi-10 composites exhibited a higher content of Ti^{3+} and O_v .

3.2. Optical Properties

The optical adsorption properties of TiO_2 , InVO_4 , and InTi-x composites were evaluated by UV-vis diffuse reflectance spectroscopy, as shown in Figure 4a. For bare TiO_2 , a strong adsorption band below 400 nm was observed, which showed the intrinsic larger band gap of anatase [34] compared with that of the bare ones. The absorption edge of InTi-x composites distinctively shifted to the visible region, and the intensity of light harvesting was also enhanced. Moreover, the band gap of TiO_2 , InVO_4 , and InTi-10 can be calculated through the converted Tauc plots, which are 3.48 eV, 2.18 eV, and 2.26 eV, respectively (Figure 4b). In addition, the Mott-Schotky measurements were investigated on TiO_2 and InVO_4 (Figure 4c,d), which indicated that both belong to the n-type semiconductor with the flatband potentials -0.25 and -0.37 V, respectively [35,36]. Finally, the conduction band edge can be calculated as 3.23 and 1.81 V, indicating a reasonable transfer of photogenerated charges occurred between TiO_2 and InVO_4 based the different energy band structure.

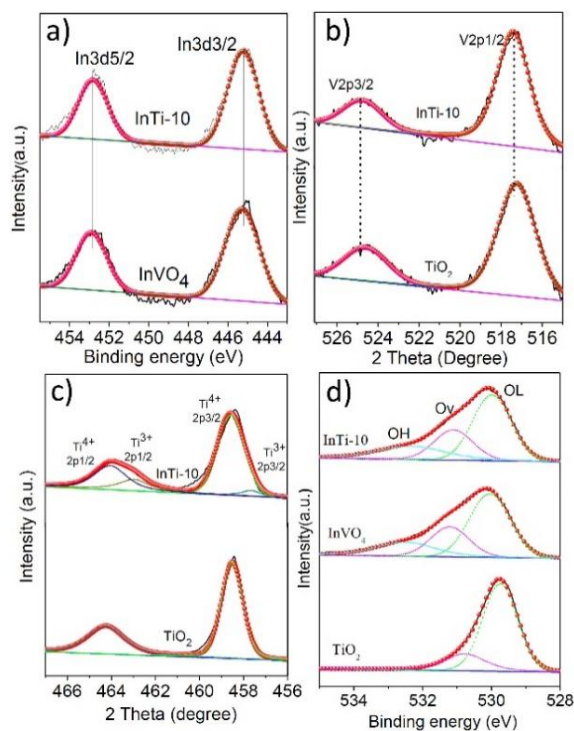


Figure 3. XPS peaks of InVO₄, TiO₂, and InTi-10 composites: (a) In 3d; (b) V 2p; (c) Ti 2p; (d) O1s.

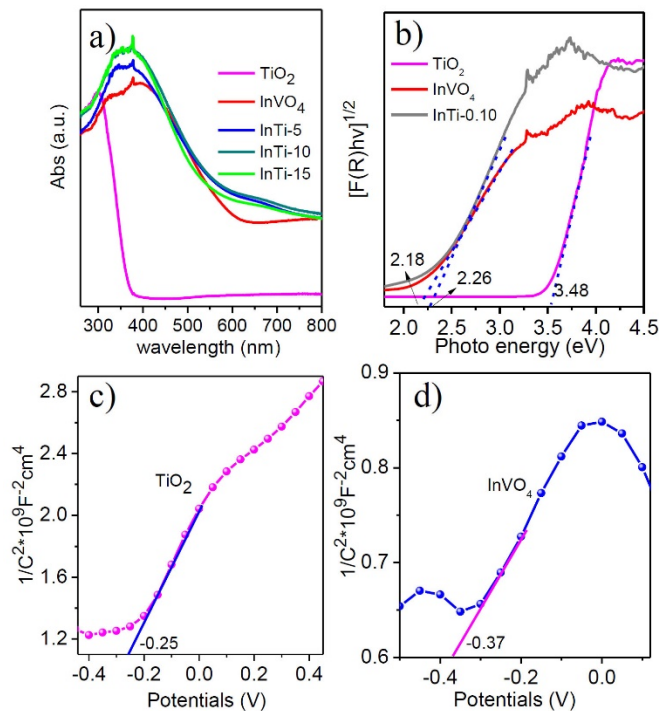


Figure 4. (a) UV-vis diffuse reflection spectra, (b) corresponding plots of $(\alpha h\nu)^{1/2}$ vs. photo energy of InVO₄, TiO₂, and InTi-x composites. Mott-Schottky plots of (c) TiO₂ and (d) InVO₄.

Photoluminescence (PL) spectroscopy was performed to reveal the separation efficiency of photogenerated charges, as shown in Figure 5a. The shape and position of emission peaks of InTi-x composites are similar to bare TiO₂ and InVO₄. Moreover, InTi-10 exhibited weakest the peak intensity, illustrating that the recombination of photogenerated electron-hole pairs is suppressed efficiently [37]. Figure 5b gives the photocurrent-time curves for TiO₂, InVO₄, and InTi-x composites. InTi-x composites showed enhanced pho-

to current density compared with that of the bare TiO_2 and InVO_4 for several on–off cycles; moreover, InTi-10 exhibited the highest photocurrent density, indicating that InTi-10 can quite effectively promote the separation and transfer of photoinduced charge carriers [38]. Electrochemical impedance spectroscopy (EIS) was further conducted to study the transfer and separation efficiency of photogenerated charges, and the obtained Nyquist diagram and the fitting results are indicated in Figure 5c,d. Generally, each arc represents a resistance during the charge transfer process and a smaller radius associated with a lower charge-transfer resistance. InTi-10 composites had the smallest diameter and exhibited the fastest charge separation and transfer [39]. Therefore, it is reasonable to conclude that InTi-10 composites showed excellent photocatalytic performance based on these photo-response measurements.

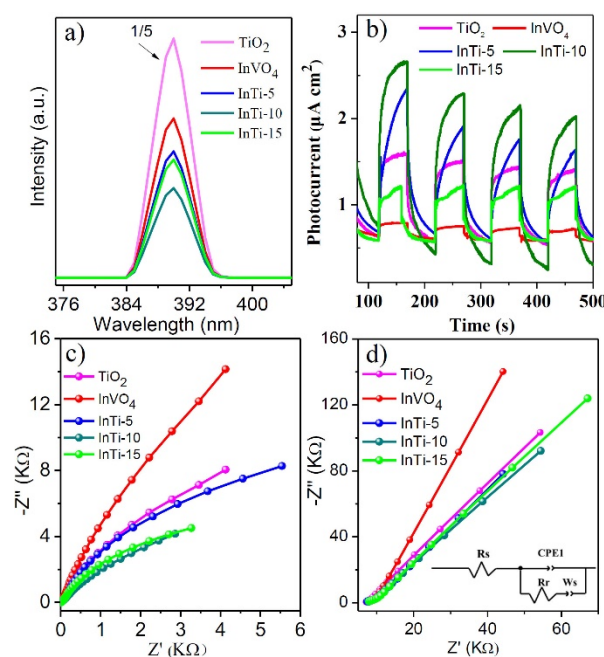


Figure 5. (a) PL spectra, (b) transient photocurrent spectra, (c) EIS Nyquist plots, and (d) impedance plots of InVO_4 , TiO_2 , and $\text{InVO}_4/\text{TiO}_2$ composites.

3.3. Photo-Oxidation of Benzyl Alcohol

The catalytic performance of the as-prepared photocatalysts was conducted in photocatalytic oxidation benzyl alcohol (BA). The results are depicted in Figure 6a. Only the product of BAD was detected in the whole reaction process. It is worth mentioning that no BA conversion was found without light irradiation or catalysts. The bare TiO_2 is almost inert in BA photocatalysis with a reaction of 3 h. After coupling with InVO_4 , all InTi-x composites exhibited higher performance. Among these catalysts, InTi-10 composites showed the best BA conversion (100%) and the highest formation rate ($3.03 \text{ mmol g}^{-1} \text{ h}^{-1}$). The above result indicate that the content of InVO_4 has an important effect on the photocatalytic performance, and the optimum percentage content is 10%. Furthermore, the cycle stability of InTi-10 composites for the photocatalytic oxidation of BA was also investigated, and no apparent loss appeared after four consecutive tests, indicating stable activity of the composite photo-catalysts. A radical trapping experiment was carried out on InTi-10 composites for the study of the main active species. Isopropanol (IPA), ammonium oxalate (AO), and benzoquinone (BQ) were used as scavengers for hydroxyl radicals ($\cdot\text{OH}$), holes (h^+), and superoxide radicals ($\cdot\text{O}_2^-$), respectively [39]. As displayed in Figure 6c, the conversion of benzyl alcohol was significantly decreased after the addition of BQ, AO, and BQ, respectively implying that $\cdot\text{O}_2^-$, $\cdot\text{OH}$, and h^+ should be the main catalytically active species for benzyl alcohol conversion.

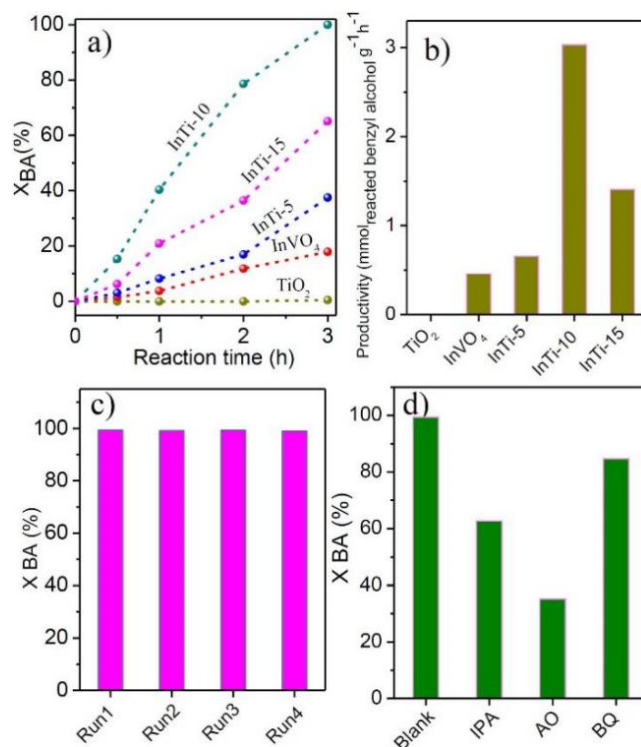


Figure 6. (a) Conversion of BA as a function of reaction time, and (b) productivity over InVO₄, TiO₂, and InVO₄/TiO₂ composites; (c) recyclability and (d) reactive species trapping tests over the InTi-10 photocatalyst.

Finally, a tentative reaction mechanism for aerobic oxidation of benzyl alcohol over InTi-*x* nanocomposites is proposed (Figure 7). The *n-n* heterojunction was formed at the interface between InVO₄(200) and TiO₂(110). Under built-in electric field driving, the photogenerated holes accumulated on the CB of TiO₂ were transferred to CB of InVO₄ for taking part in the oxidation of BA, while, the photoexcited electron easily transferred from VB of InVO₄ to VB of TiO₂ for reducing the adsorbed O₂ of reactive oxygen species. Next, the adsorbed benzyl alcohol molecules on the surface of composites were oxidized by the photogenerated holes and ·O₂⁻ species to result in the final product of benzaldehyde [40].

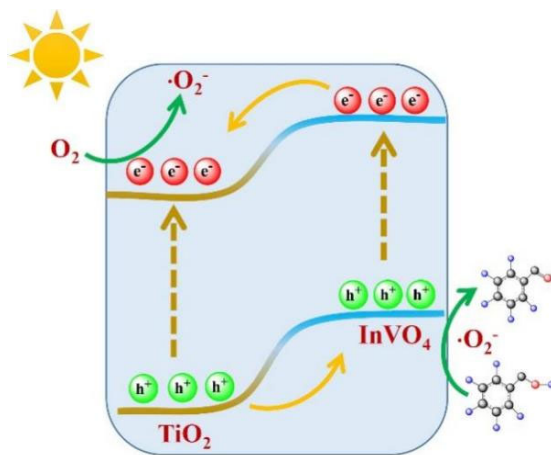


Figure 7. Schematic illustration of photoelectron-hole pair separation mechanism for InVO₄/TiO₂ under light illumination.

4. Discussion

In summary, we rationally designed and constructed a InVO₄/TiO₂ heterojunction composite via an in situ hydrothermal method. A series of characterization techniques were performed to indicate the successful fabrication of an n-n heterojunction. The InVO₄(112)/TiO₂(101) heterogeneous interface largely promoted the separation and transfer of photogenerated charges. Compared to bare TiO₂ and InVO₄, InTi-x composites exhibited a higher separation and transfer efficiency of the photogenerated charge and achieved a higher catalysis performance. InTi-10 composites gave a 100% benzyl alcohol conversion, with over 99% selectivity of benzaldehyde after a reaction of 3 h. This work provides an efficient method for the design of photocatalytic composites for the photo-oxidation of alcohols to aldehydes.

Author Contributions: Investigation, X.Z. and Q.S.; resources, J.L., Q.S. and H.D.; writing—original draft preparation, X.Z., Q.S. and H.X.; writing—review and editing, X.L. and G.L.; supervision, Q.S., H.X. and G.L.; project administration, X.L., H.X. and G.L. All authors have read and agreed to the published version of the manuscript.

Funding: We are grateful for financial support from the National Natural Science Foundation of China (22065029 and 22172167), Young Talents of Science and Technology in Universities of Inner Mongolia Autonomous Region (NJYT-20-B20), and Natural Science Foundation of Jiangxi Province (20204BCJL23039, 20192ACBL21027).

Data Availability Statement: Data are contained within the article.

Conflicts of Interest: The authors declare no conflict of interest.

References

1. Chu, S.; Majumdar, A. Opportunities and challenges for a sustainable energy future. *Nature* **2012**, *488*, 294–303. [[CrossRef](#)] [[PubMed](#)]
2. Shi, Q.Q.; Wei, X.J.; Raza, A.; Li, G. Recent advances in aerobic photo-oxidation of methanol to valuable chemicals. *ChemCatChem* **2020**, *13*, 3381–3395. [[CrossRef](#)]
3. Shen, Z.; Hua, Y.; Li, B.; Zou, Y.; Li, S.; Busser, G.; Wang, X.; Zhao, G.; Muhler, M. State-of-the-art progress in the selective photo-oxidation of alcohols. *J. Energy Chem.* **2021**, *62*, 338–350. [[CrossRef](#)]
4. Campisi, S.; Ferri, M.; Chan-Thaw, C.; Trujillo, F.; Motta, D.; Tabanelli, T.; Dimitratos, N.; Villa, A. Metal-support cooperative effects in Au/VPO for the aerobic oxidation of benzyl alcohol to benzyl benzoate. *Nanomaterials* **2019**, *9*, 299. [[CrossRef](#)]
5. Shi, Q.; Qin, Z.; Yu, C.; Waheed, A.; Xu, H.; Gao, Y.; Abroshan, H.; Li, G. Experimental and mechanistic understanding of photo-oxidation of methanol catalyzed by CuO/TiO₂-spindle nanocomposite: Oxygen vacancy engineering. *Nano Res.* **2020**, *13*, 939–946. [[CrossRef](#)]
6. Hu, Y.; Yu, X.H.; Liu, Q.Q.; Wang, L.L.; Tang, H. Highly metallic Co-doped MoS₂ nanosheets as an efficient cocatalyst to boost photoredox dual reaction for H₂ production and benzyl alcohol oxidation. *Carbon* **2022**, *188*, 70–80. [[CrossRef](#)]
7. Qin, Z.; Hu, S.; Han, W.; Li, Z.; Xu, W.W.; Zhang, J.; Li, G. Tailoring optical and photocatalytic properties by single-Ag-atom exchange in Au₁₃Ag₁₂(PPh₃)₁₀Cl₈ nanoclusters. *Nano Res.* **2022**, *15*, 2971–2976. [[CrossRef](#)]
8. Verma, R.; Potter, M.E.; Oakley, A.E.; Mhembere, P.M.; Raja, R. Bimetallic PdAu catalysts within hierarchically porous architectures for aerobic oxidation of benzyl alcohol. *Nanomaterials* **2021**, *11*, 350. [[CrossRef](#)]
9. Qi, M.; Conte, M.; Anpo, M.; Tang, Z.; Xu, Y. Cooperative coupling of oxidative organic synthesis and hydrogen production over semiconductor-based photocatalysts. *Chem. Rev.* **2021**, *21*, 13051–13085. [[CrossRef](#)]
10. Li, J.Q.; Li, F.P.; Yang, Q.; Wang, S.B.; Sun, H.Q.; Yang, Q.N.; Tang, J.W.; Liu, S.M. Tailoring collaborative N-O functionalities of graphene oxide for enhanced selective oxidation of benzyl alcohol. *Carbon* **2021**, *182*, 715–724. [[CrossRef](#)]
11. Guo, Q.; Zhou, C.Y.; Ma, Z.B.; Yang, X.M. Fundamentals of TiO₂ photocatalysis: Concepts, mechanisms, and challenges. *Adv. Mater.* **2019**, *31*, 1901997. [[CrossRef](#)]
12. Shi, Q.; Ping, G.; Wang, X.; Xu, H.; Li, J.; Cui, J.; Abroshan, H.; Ding, H.; Li, G. CuO/TiO₂ heterojunction composites: An efficient photocatalyst for selective oxidation of methanol to methyl formate. *J. Mater. Chem. A* **2019**, *7*, 2253–2260. [[CrossRef](#)]
13. Oliveira, M.; Rivelino, R.; Mota, F.; Gueorguiev, G. Optical properties and quasiparticle band gaps of transition-metal atoms encapsulated by silicon cages. *J. Phys. Chem. C* **2014**, *118*, 5501–5509. [[CrossRef](#)]
14. Meng, A.Y.; Zhang, L.Y.; Cheng, B.; Yu, J.G. Dual cocatalysts in TiO₂ photocatalysis. *Adv. Mater.* **2018**, *31*, 1807660.
15. Medeiros, P.V.; Gueorguiev, G.K.; Stafström, S. Bonding, charge rearrangement and interface dipoles of benzene, graphene, and PAH molecules on Au(111) and Cu(111). *Carbon* **2015**, *81*, 620–628. [[CrossRef](#)]
16. Yang, R.J.; Zhang, Y.F.; Fan, Y.Y.; Wang, R.H.; Zhu, R.S.; Tang, Y.X.; Yin, Z.Y.; Zeng, Z.Y. InVO₄-based photocatalysts for energy and environmental applications. *Chem. Eng. J.* **2022**, *428*, 131145. [[CrossRef](#)]

17. Perales-Martínez, I.A.; Rodríguez-González, V.; Lee, S.W.; Obregón, S. Facile synthesis of InVO₄/TiO₂ heterojunction photocatalysts with enhanced photocatalytic properties under UV-vis irradiation. *J. Photoch. Photobiol. A* **2015**, *299*, 152–158. [[CrossRef](#)]
18. Zhang, J.; Wang, J.; Zhu, Q.J.; Zhang, B.B.; Xu, H.H.; Duan, J.Z.; Hou, B.R. Fabrication of a novel AgBr/Ag₂MoO₄@InVO₄ composite with excellent visible light photocatalytic property for antibacterial use. *Nanomaterials* **2020**, *10*, 1541. [[CrossRef](#)]
19. Shi, Q.; Li, Y.; Zhou, Y.; Miao, S.; Ta, N.; Zhan, E.; Liu, J.; Shen, W. The shape effect of TiO₂ in VO_x/TiO₂ catalysts for selective reduction of NO by NH₃. *J. Mater. Chem. A* **2015**, *3*, 14409–14415. [[CrossRef](#)]
20. Fan, Y.Y.; Yang, R.J.; Zhu, R.S.; Zhu, Z.Y. CdS decorated artificial leaf BiVO₄/InVO₄ for photocatalytic hydrogen production and simultaneous degradation of biological hydrogen production wastewater. *Catal. Today* **2021**, *364*, 190–195. [[CrossRef](#)]
21. Zayed, M.; Samy, S.; Shaban, M.; Altowyan, A.S.; Hamdy, H.; Ahmed, A.M. Fabrication of TiO₂/NiO p-n nanocomposite for enhancement dye photodegradation under solar radiation. *Nanomaterials* **2022**, *12*, 989. [[CrossRef](#)] [[PubMed](#)]
22. Shi, W.L.; Guo, F.; Chen, J.B.; Che, G.B.; Lin, X. Hydrothermal synthesis of InVO₄/graphitic carbon nitride heterojunctions and excellent visible-light-driven photocatalytic performance for rhodamine B. *J. Hazard. Mater.* **2014**, *612*, 143–148. [[CrossRef](#)]
23. Dalto, F.; Kuźniarska-Biernacka, I.; Pereira, C.; Mesquita, E.; Soares, O.S.G.P.; Pereira, M.F.R.; Rosa, M.J.; Mestre, A.S.; Carvalho, A.P.; Freire, C. Solar light-induced methylene blue removal over TiO₂/AC composites and photocatalytic regeneration. *Nanomaterials* **2021**, *11*, 3016. [[CrossRef](#)]
24. Wang, Y.; Jiang, Q.; Xu, L.; Han, Z.-K.; Guo, S.; Li, G.; Baiker, A. Effect of Configuration of Copper Oxide-Ceria Catalysts in NO Reduction with CO: Superior Performance of Copper-Ceria Solid Solution. *ACS Appl. Mater. Interfaces* **2021**, *13*, 61078–61087. [[CrossRef](#)] [[PubMed](#)]
25. Zhang, X.; Li, Z.; Pei, W.; Li, G.; Liu, W.; Du, P.; Wang, Z.; Qin, Z.; Qi, H.; Liu, X.; et al. Crystal Phase Mediated Restructuring of Pt on TiO₂ with Tunable Reactivity: Redispersion versus Reshaping. *ACS Catal.* **2022**, *12*, 3634–3643. [[CrossRef](#)]
26. Hafeez, H.Y.; Lakhera, S.K.; Ashokkumar, M.; Neppolian, B. Ultrasound assisted synthesis of reduced graphene oxide (rGO) supported InVO₄-TiO₂ nanocomposite for efficient Hydrogen production. *Ultrason. Sonochem.* **2019**, *53*, 1–10. [[CrossRef](#)] [[PubMed](#)]
27. Hafeez, H.Y.; Lakhera, S.K.; Shankar, M.V.; Neppolian, B. Synergetic improvement in charge carrier transport and light harvesting over ternary InVO₄-g-C₃N₄/rGO hybrid nanocomposite for hydrogen evolution reaction. *Int. J. Hydrog. Energy* **2019**, *45*, 7530–7540. [[CrossRef](#)]
28. Li, L.; Yang, Y.; Yang, L.Q.; Wang, X.Y.; Zhou, Y.; Zou, Z.G. 3D hydrangea-like InVO₄/Ti₃C₂T_x hierarchical heterosystem collaborating with 2D/2D interface interaction for enhanced photocatalytic CO₂ reduction. *ChemNanoMat* **2021**, *7*, 1–10. [[CrossRef](#)]
29. Zhang, S.W.; Gong, X.; Shi, Q.Q.; Ping, G.C.; Xu, H.; Waleed, A.; Li, G. CuO nanoparticle-decorated TiO₂-nanotube heterojunctions for direct synthesis of methyl formate via photo-oxidation of methanol. *ACS Omega* **2020**, *5*, 15942–15948. [[CrossRef](#)]
30. Cao, Y.; Su, Y.; Xu, L.; Yang, X.; Han, Z.; Cao, R.; Li, G. Ionic liquids modified oxygen vacancy-rich amorphous FeNi hydroxide nanoclusters on carbon-based materials as an efficient electrocatalyst for electrochemical water oxidation. *J. Energy Chem.* **2022**, *71*, 167–173. [[CrossRef](#)]
31. Yu, X.; Fan, X.; An, L.; Liu, G.; Li, Z.; Liu, J.; Hu, P. Mesocrystalline Ti³⁺-TiO₂ hybridized g-C₃N₄ for efficient visible-light photocatalysis. *Carbon* **2018**, *128*, 21–30. [[CrossRef](#)]
32. Shi, Q.Q.; Wang, Y.H.; Guo, S.; Han, Z.K.; Ta, N.; Li, G.; Baiker, A. NO reduction with CO over CuO_x/CeO₂ nanocomposites: Influence of oxygen vacancies and lattice strain. *Catal. Sci. Technol.* **2021**, *11*, 6543–6552. [[CrossRef](#)]
33. Li, Z.M.; Zhang, X.Y.; Shi, Q.Q.; Gong, X.; Xu, H.; Li, G. Morphology effect of ceria supports on gold nanocluster catalyzed CO oxidation. *Nanoscale Adv.* **2021**, *3*, 7002–7006. [[CrossRef](#)]
34. Li, Y.; Zhang, M.Q.; Liu, Y.F.; Sun, Y.X.; Zhao, Q.H.; Chen, T.L.; Chen, Y.F.; Wang, S.F. In situ construction of bronze/anatase TiO₂ homogeneous heterojunctions and their photocatalytic performances. *Nanomaterials* **2022**, *12*, 1122. [[CrossRef](#)]
35. Chen, C.; Li, M.; Jia, Y.; Chong, R.; Xu, L.; Liu, X. Surface defect-engineered silver silicate/ceria p-n heterojunctions with a flower-like structure for boosting visible light photocatalysis with mechanistic insight. *J. Colloid Interface Sci.* **2020**, *564*, 442–453. [[CrossRef](#)]
36. Makuła, P.; Pacia, M.; Macyk, W. How to correctly determine the band gap energy of modified semiconductor photocatalysts based on UV-Vis spectra. *J. Phys. Chem. Lett.* **2018**, *9*, 6814–6817. [[CrossRef](#)]
37. Song, Y.; Lu, X.; Liu, Z.B.; Liu, W.F.; Gai, L.G.; Gao, X.; Ma, H.F. Efficient removal of Cr(VI) by TiO₂ based micro-manometer reactor via the synergy of adsorption and photocatalysis. *Nanomaterials* **2022**, *12*, 291. [[CrossRef](#)]
38. Tang, S.F.; Yin, X.P.; Wang, G.Y.; Lu, X.L.; Lu, T.B. Single titanium-oxide species implanted in 2D g-C₃N₄ matrix as a highly efficient visible-light CO₂ reduction photocatalyst. *Nano Res.* **2021**, *12*, 457–462. [[CrossRef](#)]
39. Bao, X.L.; Li, H.L.; Wang, Z.Y.; Tong, F.X.; Liu, M.; Zheng, Z.K.; Wang, P.; Cheng, H.F.; Liu, Y.Y.; Dai, Y.; et al. TiO₂/Ti₃C₂ as an efficient photocatalyst for selective oxidation of benzyl alcohol to benzaldehyde. *Appl. Catal. B* **2021**, *286*, 119885. [[CrossRef](#)]
40. Waheed, A.; Cao, C.; Zhang, Y.; Zheng, K.; Li, G. Insight into Au/ZnO Catalyzed Aerobic Benzyl Alcohol Oxidation by Modulation-Excitation Attenuated Total Reflection IR Spectroscopy. *New J. Chem.* **2022**, *46*, 5361–5367. [[CrossRef](#)]